

Contents lists available at ScienceDirect

# **Tectonophysics**

journal homepage: www.elsevier.com/locate/tecto



# Experimental measurements of anisotropic viscosity in naturally sourced dunite with a preexisting CPO

Cameron D. Meyers \*,1, David L. Kohlstedt

Department of Earth and Environmental Sciences, University of Minnesota, Minneapolis, MN, USA

#### ABSTRACT

Naturally deformed dunite cores with a preexisting crystallographic preferred orientation (CPO), collected from a shear zone in the Josephine peridotite (southwest Oregon, USA), were deformed experimentally in triaxial compression. The compression axis was varied relative to the CPO geometry to measure the anisotropy in viscosity of these rocks. Deformation experiments were performed in a gas-medium apparatus at three constant displacement-rate steps, at a temperature of  $1250\,^{\circ}$ C and a confining pressure of 300 MPa. Cores were dehydrated at  $1200\,^{\circ}$ C in a controlled CO/CO<sub>2</sub> atmosphere prior to deformation to achieve nominally dry conditions. Data from individual experiments were fit by a power-law, yielding a stress exponent of  $n \approx 3.6$ , indicative of deformation by dislocation creep. The maximum difference in viscosity was a factor of 2.6 at constant stress. The CPO of the olivine grains was measured after deformation by electron backscatter diffraction (EBSD). The flow stress correlated with the mean Schmid factor (or resolved shear stress) on the easiest dislocation slip systems, calculated from grain orientations determined from EBSD analyses. Analysis of our data with a simplified effective-medium model, which incorporated constraints from published single-crystal flow laws, demonstrated the link between CPO and anisotropy in viscosity. Predictions from viscoplastic self-consistent (VPSC) models support our simplified analysis of the measured anisotropy.

# 1. Introduction

Grain-scale deformation in Earth's upper mantle allows convective flow that leads to plate-scale crystallographic alignment of olivine and other minerals, reflecting deformation kinematics. This crystallographic preferred orientation (CPO) imparts anisotropic physical properties to the upper mantle due to the anisotropic, orthorhombic crystal structure of the primary mineral, olivine. Distinct olivine CPOs are often observed in naturally deformed olivine-rich mantle rocks collected at Earth's surface from localities such as tectonically exhumed ophiolites and mantle xenoliths ejected by volcanism (Ismail and Mainprice, 1998; Mehl et al., 2003; Warren et al., 2008; Skemer et al., 2013; Chatzaras et al., 2016). Seismic detection of elastic anisotropy provides strong evidence that olivine CPOs are pervasive throughout Earth's upper mantle (Long and Silver, 2009; Long and Becker, 2010). Magnetotelluric data similarly show plate-scale anisotropic electrical conductivity in the upper mantle (Gatzemeier and Moorkamp, 2005; Gatzemeier and Tommasi, 2006). Calculated seismic anisotropy from numerical models that combine grain-scale CPO formation and finite strain estimated from plate motions correlate well with measured seismic anisotropy, reinforcing the inference that the CPO of olivine is the underlying cause of upper mantle anisotropy (Tommasi, 1998; Becker et al., 2003; Becker

# et al., 2006).

High-temperature deformation experiments on olivine-rich rocks have reproduced olivine CPO formation in the laboratory by imposing high strains in torsion or in general (approximately simple) shear between angled pistons (Jung and Karato, 2001; Bystricky et al., 2000; Katayama et al., 2004; Hansen et al., 2012a; Hansen et al., 2012b; Hansen et al., 2014; Tasaka et al., 2015; Tielke et al., 2016a). Typically, alignment of the easiest (weakest) dislocation slip system is thought to control CPO geometry. This conclusion is supported by experiments on olivine single crystals that quantify the relative strengths of the slip systems in olivine (Durham and Goetze, 1977; Ricoult and Kohlstedt, 1985; Bai et al., 1991; Bai and Kohlstedt, 1992; Tielke et al., 2016b). Four dominant slip systems have been identified: (010)[100], the paired (001)[100] and (100)[001], and (010)[001], listed in order of their relative weakness under dry upper mantle conditions. At these conditions, at a given stress, the strain rate differs by more than two orders of magnitude between the weakest and strongest slip systems. Such significant mechanical anisotropy leads to the prediction that an olivinerich rock with a pronounced CPO should have strongly anisotropic viscosity as well.

Most geodynamic models of upper mantle flow do not account for anisotropic viscosity. However, depending on its magnitude, ignoring

 $<sup>^{\</sup>star}$  Corresponding author.

E-mail address: cameron meyers@brown.edu (C.D. Meyers).

<sup>&</sup>lt;sup>1</sup> Present Address: Department of Earth, Environmental, and Planetary Sciences, Brown University, 324 Brook St, Providence, RI 02912, USA.

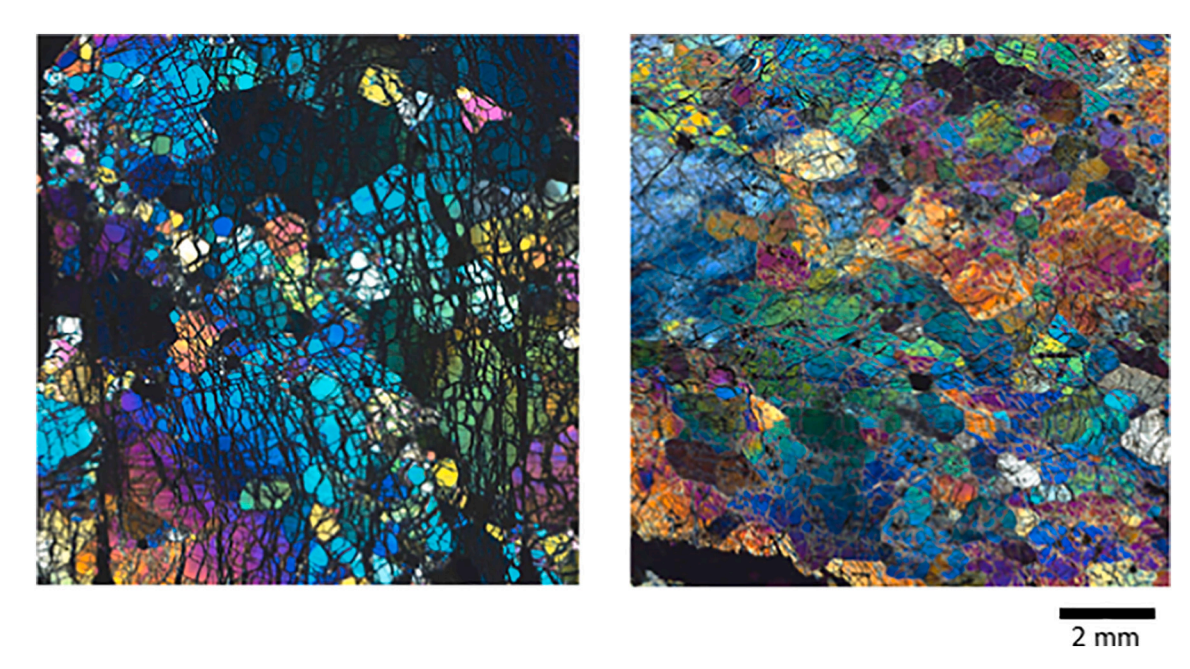


Fig. 1. Cross-polarized optical micrographs of thin-sections prepared from dehydrated, undeformed material (left) and statically annealed, deformed material (right).

anisotropy may result in large errors when modeling dynamic processes (Pouilloux et al., 2007). Numerical simulations demonstrate that viscous anisotropy influences the spacing and timing of Rayleigh-Taylor instabilities, the thermal structure of the mantle wedge in subduction zones, the rate and geometry of post-glacial rebound, the shape and flow distribution of convection cells, and the geometry of lithospheric shear zones (Christensen, 1987; Han and Wahr, 1997; Lev and Hager, 2008; Tommasi et al., 2009; Lev and Hager, 2011). Multiscale models, incorporating experimentally determined strengths for different slip systems, indicate a viscosity ratio of 1.5–3 between the strongest and weakest orientations of polycrystalline olivine with a CPO resulting from simulated high-strain deformation (Knoll et al., 2009; Tommasi et al., 2009).

Direct experimental measurements of the anisotropy of viscosity in textured olivine aggregates are limited. Wendt et al. (1998) performed axial compression experiments on naturally textured peridotites, deformed in different orientations relative to their preexisting foliation. These experiments were conducted on natural specimens collected from several locations and were experimentally deformed in a semi-brittle regime where high stress exponents (n=5-25) were measured, such that viscous anisotropy was not easily quantified. In another set of studies, hot-pressed, iron-rich olivine aggregates were deformed in either torsion or axial extension, followed by deformation in the alternate geometry (Hansen et al., 2012b; Hansen et al., 2016a; Hansen et al., 2016b). These experiments yielded a maximum viscosity ratio of 14 at constant stress.

In the present study, samples prepared from a hand sample of naturally deformed dunite collected from a shear zone in the Josephine peridotite were experimentally deformed at high temperature in several different orientations relative to its preexisting CPO. Strain-rate stepping experiments were used to measure the strength of the rock in different orientations and thus quantify the anisotropy in viscosity. A simple mechanical model, incorporating weighted Schmid factors (resolved shear stress) for each of the dominant slip systems, was compared to the data to extend the results to broader application. While experimental deformation of naturally exhumed rocks brings about technical challenges that are avoided when using synthetic rocks, these experiments provide a framework for quantifying anisotropic viscosity in Earth's upper mantle and for verifying that CPO imparts anisotropic viscosity to naturally deformed dunites. Further, due to the coarse grain size and

high experimental temperatures, these samples are expected to deform by dislocation creep, while previous experiments on hot-pressed olivine aggregates were deformed in the dislocation-accommodated grain boundary sliding (disGBS) regime.

# 2. Methods

Samples of a dunite with a preexisting CPO were cored in different orientations, dehydrated at 1 atm, and deformed in a gas-medium apparatus (Paterson, 1990) to measure its viscous anisotropy. A dunite rock collected from a shear zone in the Josephine peridotite was selected as starting material. This rock was previously studied in detail by Warren et al. (2008), labeled as sample 3924J03b in their study. Based on structural field relationships, these researchers deduced that the dunite rock had undergone a shear strain of  $\sim$ 3.4. The chosen hand sample had an intermediate intensity A/D-type CPO, typical of deformation under dry conditions, with the [100] direction dominantly aligned with the shear direction and the [010] direction dominantly normal to the shear plane but somewhat girdled normal to the shear direction. The mean grain size of the chosen dunite rock is  $\sim$ 500  $\mu$ m; however, the grain size is heterogeneous, with some grains several millimeters in dimension. This coarse-grained, heterogeneous microstructure is clear from the optical micrographs of thin sections shown in Fig. 1. The dunite rock was oriented for deformation by measuring the mean orientation of the CPO from a large low-resolution (50 µm step size) EBSD map of a portion of it. Cores were then obtained along axes close to the [100], [010], [001], [110]c, and [101]c directions of the mean orientation (where the csubscript indicates use of a cubic crystallographic coordinates, as typical of experiments on olivine single crystals - see Durham and Goetze, 1977). The orientations of the axis of the cores relative to the mean orientation of the CPO are subsequently referred to as the nominal orientation of the core. These labels are useful for identifying core orientations relative to the CPO, but it is important to note that a broad range of crystallographic orientations exists in each sample. Cores with a diameter of 10 mm and a length of 12-21 mm were squared at the ends, placed in a Ni sleeve, and dehydrated for 12 h at 1200  $^{\circ}\text{C}$  in a controlledatmosphere furnace under mixed CO/CO2, with a ratio such that the oxygen partial pressure, pO2, was near the Ni/NiO buffer. Samples were hydrostatically annealed for an additional 3 h at 1250  $^{\circ}$ C and 300 MPa in

Table 1
Summary of experimental results.

Nominal orientation	Strain rate $(10^{-5} \text{ s}^{-1})$	Stress (MPa)	n	$A \text{ (MPa}^{-3.6} \text{ s}^{-1}) (n = 3.6)$	$F(A_0 = 1.1e-13)$	$S_{(010)[100]}$	$S_{(001)[100]/(100)[001]}$	$S_{(010)[001]}$
[100]	2.2	175	3.4	1.9e-13	1.7	0.21	0.20	0.09
	1.1	144						
	0.53	115						
[010]	2.2	202	3.2	1.1e-13	1.0	0.15	0.14	0.25
	1.2	166						
	0.59	134						
[001]	2.1	197	3.6	1.2e-13	1.1	0.14	0.18	0.31
	1.1	166						
	0.53	134						
[110] <sub>c</sub>	2.0	150	3.9	2.9e-13	2.6	0.27	0.22	0.21
	1.1	128						
	0.60	110						
[101] <sub>c</sub>	2.1	164	3.9	2.2e-13	2.0	0.19	0.18	0.22
	1.1	140						
	0.56	116						
		Mean:	3.6					

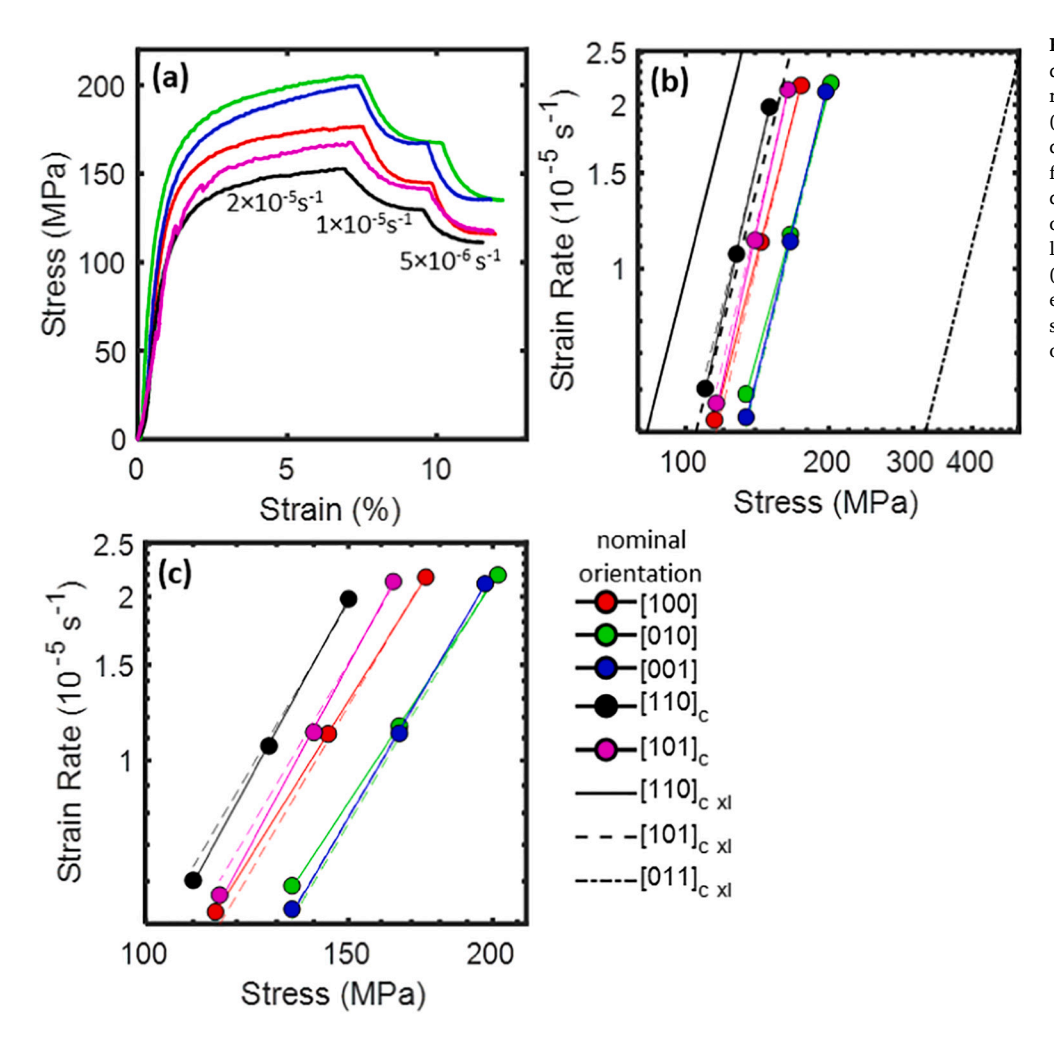


**Fig. 2.** Mechanical data measured from deformation experiments. (a) Stress-strain records labeled with nominal strain rates. (b) Stress versus strain rate measured for dunite samples compared to single-crystal flow laws. Solid colored lines are fits of the data to a power-law equation, and dotted colored lines are fits of the data to a power law with the stress exponent fixed at n = 3.6. (c) Stress versus strain rate measured from experiments, highlighting differences in strength between experiments on differently orientated cores.

the deformation apparatus, prior to deformation.

Axial compression experiments were performed at 1250 °C and 300 MPa in a gas-medium apparatus (Paterson, 1990) under constant displacement-rate conditions at three rates. Nominal strain-rates of  $2\times 10^{-5},\,1\times 10^{-5},\,$  and  $5\times 10^{-6}\,$  s $^{-1}$  were applied, allowing the stress to stabilize to a nearly steady-state value at each step. Each sample was deformed to a total strain of less than 12% with calculated stresses between 110 and 202 MPa (see Table 1). This approach for quantifying the mechanical properties of natural dunites is very similar to that taken by

#### Chopra and Paterson (1984).

After deformation, samples were cut parallel to the compression axis in preparation for EBSD analyses. Sections were polished progressively on diamond lapping film to a final grit size of 0.5  $\mu m$ , followed by polishing with colloidal silica (Syton). EBSD data were collected using a JEOL 6500 field emission SEM using Oxford Aztek software, which was then processed with the MTEX toolbox (Bachmann et al., 2010). EBSD maps were collected of an entire section (cut along the deformation axis) of each sample at a 10  $\mu m$  step size. Non-indexed points with five or

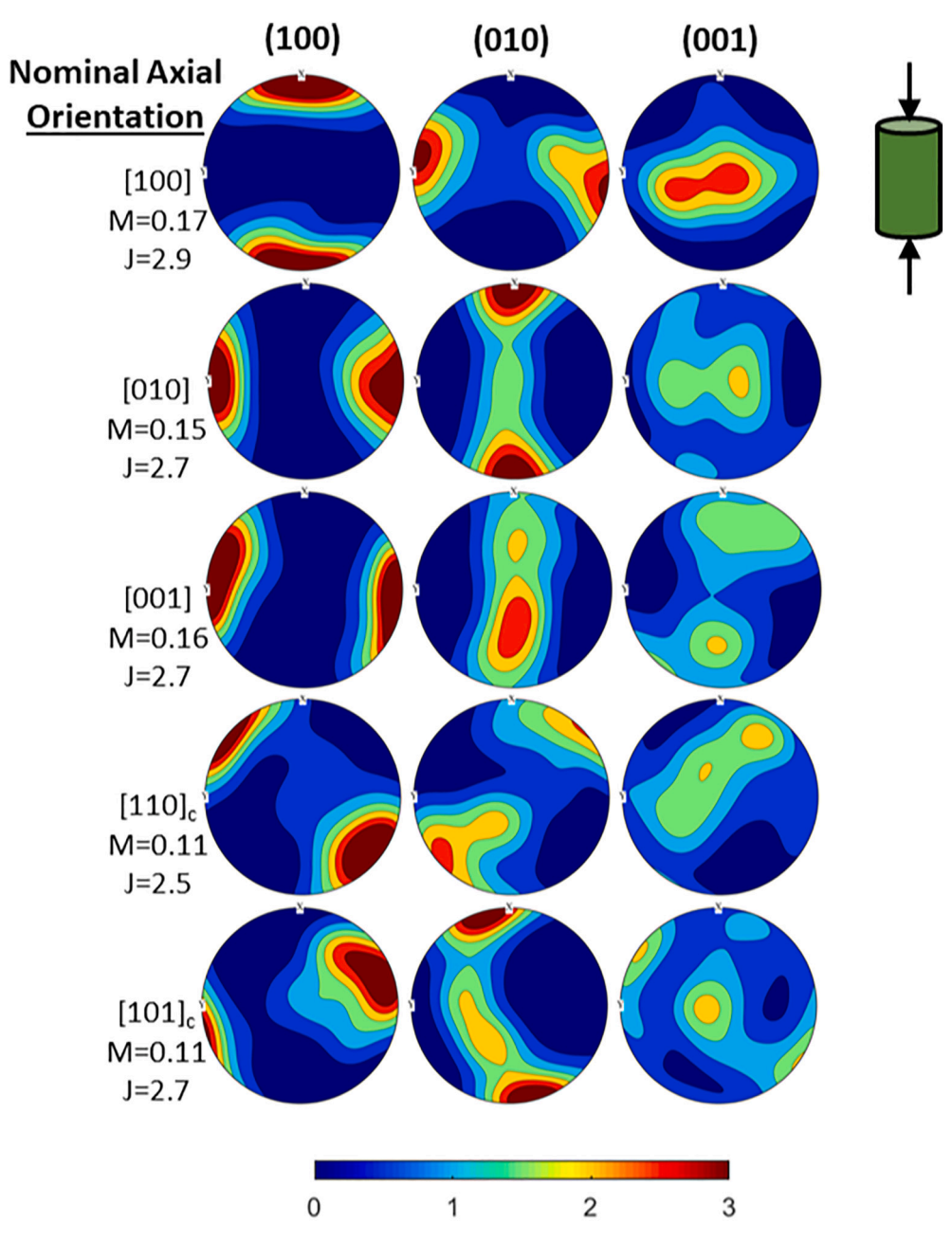


Fig. 3. Pole figures calculated from EBSD maps of deformed samples in the specimen reference frame.

more neighboring points belonging to a single grain were interpolated. Schmid factors were calculated for the (010)[100], (010)[001], (001)[100], and (100)[001] slip systems from these maps, which were used in fitting a mechanical model designed to describe the viscous anisotropy of these samples.

# 3. Results

Anisotropic strength was measured during high-temperature deformation of cores of natural dunites with preexisting CPOs. The stress measured at the same nominal strain rate varied among samples. Stress–strain curves from each experiment are presented in Fig. 2a. In each case, samples yielded at relatively low strain, then harden to a nearly steady-state stress at  $\sim\!7\%$  strain at the fastest applied strain rate. Upon stepped reduction of strain rate, samples relaxed to a new, nearly steady-state value over roughly 2.5% strain for each step. The final stress from each rate step was used to fit the data from each experiment to a

power law of the form

$$\dot{\varepsilon} = A\sigma^n,\tag{1}$$

where  $\dot{e}$  is the strain-rate, A is a material-dependent prefactor,  $\sigma$  is the differential stress, and n is the stress exponent. As summarized in Fig. 2b and c, a stress exponent of n=3.2 to 3.9 was determined across all experiments, with a mean of n=3.6. This value is broadly consistent with models of deformation by dislocation creep and those reported in other studies of experimental deformation of naturally sourced coarsegrained dunites (Chopra and Paterson, 1984; Keefner et al., 2011). This value for the stress exponent is also similar to those measured from deformation of olivine single crystals and synthetic, reconstituted dunites where deformation was attributed to dislocation creep (Durham and Goetze, 1977; Bai and Kohlstedt, 1992; Hirth and Kohlstedt, 2003; Hirth and Kohlstedt, 2015; Mullet et al., 2015). If n is fixed at 3.6 so that power-law relationships for all of the samples could be directly compared, the values of the prefactor range from  $A=1.1\times 10^{-13}$ 

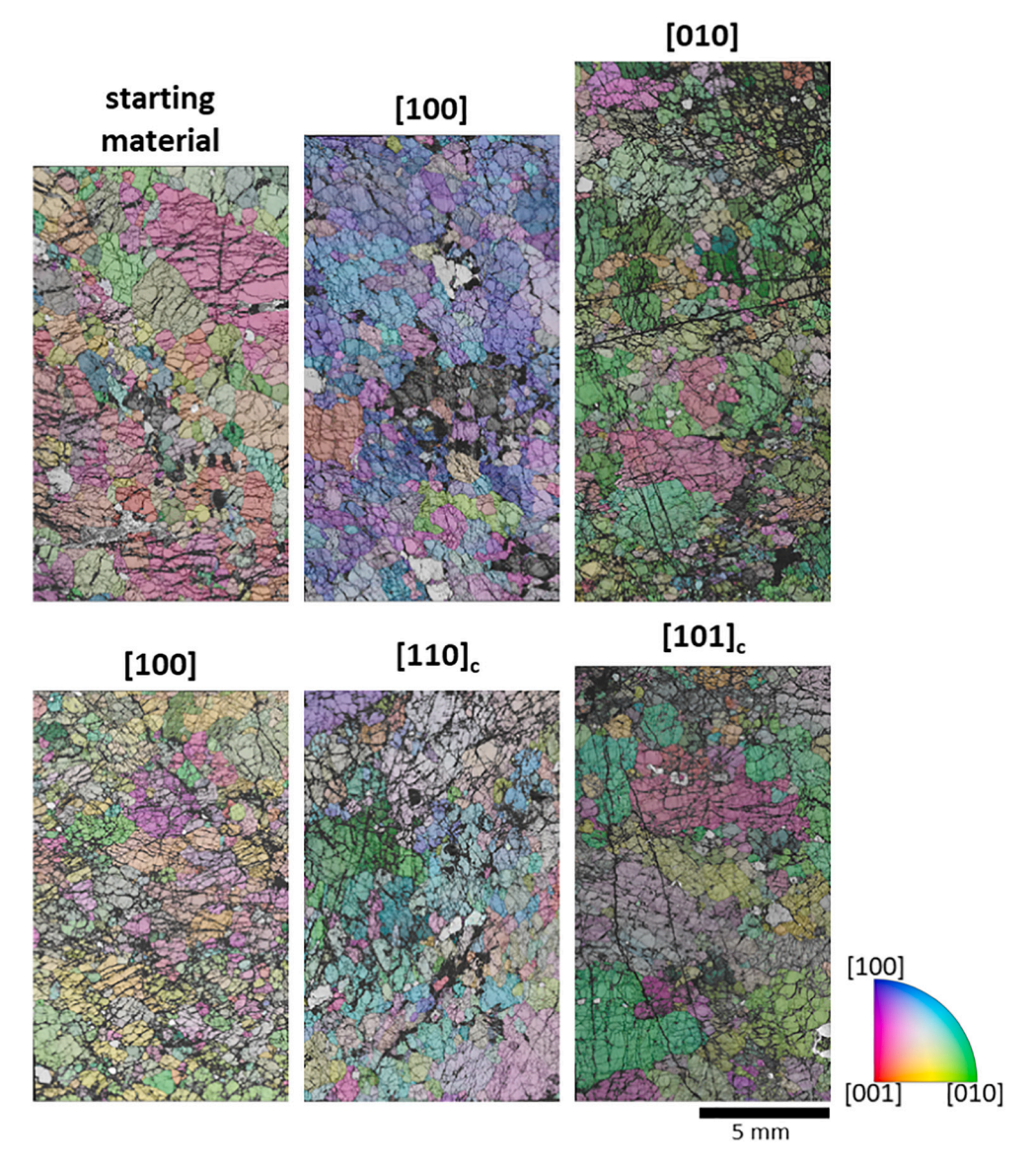


Fig. 4. EBSD maps shaded by band contrast and with superimposed inverse pole figure (IPF) coloring (referenced to the compression direction) of indexed olivine grains from dehydrated starting material and deformed samples.

MPa<sup>-3.6</sup> s<sup>-1</sup> to  $A=2.9\times10^{-13}$  MPa<sup>-3.6</sup> s<sup>-1</sup>, a factor of 2.6 difference in viscosity at the same stress between the strongest and weakest orientations tested. The data are bounded by the strengths of single crystals oriented for slip on each of the dominant slip systems and fall near the strength of single crystals in the [101]<sub>c</sub> orientation (Bai et al., 1991), Fig. 2b.

The samples have significant CPOs revealed by EBSD measurements, as summarized with the pole figures in Fig. 3. The M-index, quantifying fabric strength (Skemer et al., 2005), measured from each deformed sample ranges from M=0.11 to 0.17 (J-index =2.5–2.9), slightly less than the M-index measured from the starting material of M=0.20 (J-index =3.4). These CPO strengths are consistent with those measured previously from nearby rocks collected from the same outcrop (Warren et al., 2008). A maximum of only 12% strain was imposed during our deformation experiments, such that the measured fabric is approximately representative of the preexisting CPO of each sample with only slight modification by the experimentally imposed deformation. EBSD maps of both the dehydrated starting material and the deformed samples, reveal a microstructure containing lobate grains and a broad grain-size distribution, as demonstrated in Fig. 4. Grains are cut by pervasive relict fractures. Fracture surfaces appear to be open in the dehydrated

starting material but closed after samples are heated and deformed under confining pressure. The closure of relict fractures is also apparent in the optical micrographs presented in Fig. 1.

Maps of Schmid factor (relative resolved shear stress) for each of the primary dislocation slip systems demonstrate that samples in different orientations have broadly varying populations of grains well-oriented for slip (Fig. 5). Samples with the nominal orientations [110]<sub>c</sub> and [101]<sub>c</sub> contain many grains oriented with high resolved shear stress on the easiest slip systems, (010)[100] and the paired (001)[100] and (100) [001] (which always have the same resolved shear stress). Samples with the nominal orientations [001] and [010], however, have very few grains oriented with high resolved shear stress on these slip systems, but they do contain a significant number of grains oriented well for slip on the hard (010)[001] slip system. The sample with the nominal [100] orientation is intermediate, with some grains oriented reasonably well for slip on the two easiest slip systems and few well-oriented for slip on the hardest slip system. We emphasize that the notation of nominal orientation is useful for orienting the hand sample relative to the CPO but that each core contains a broad population of grain orientations. Given the large grain size of these samples, some sample-to-sample heterogeneity is expected, such that large-scale EBSD maps of each

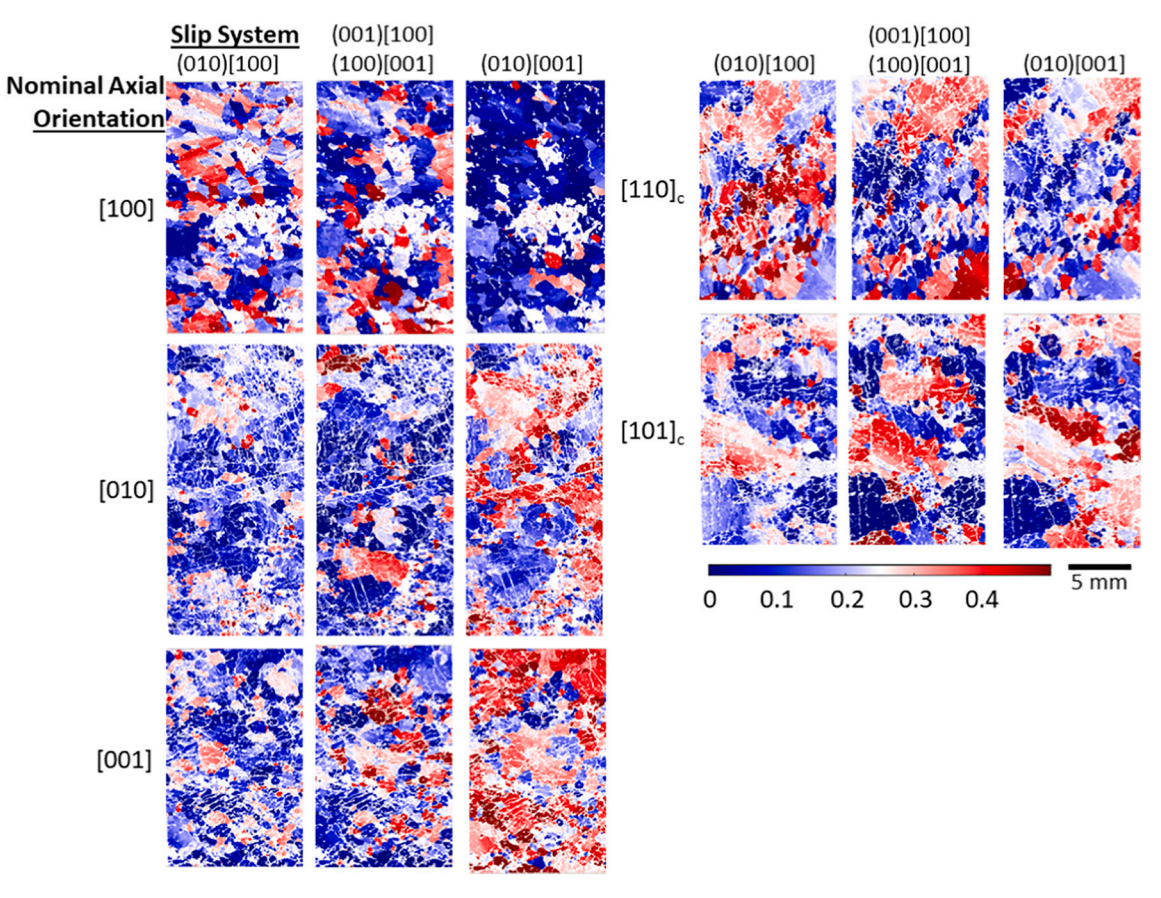
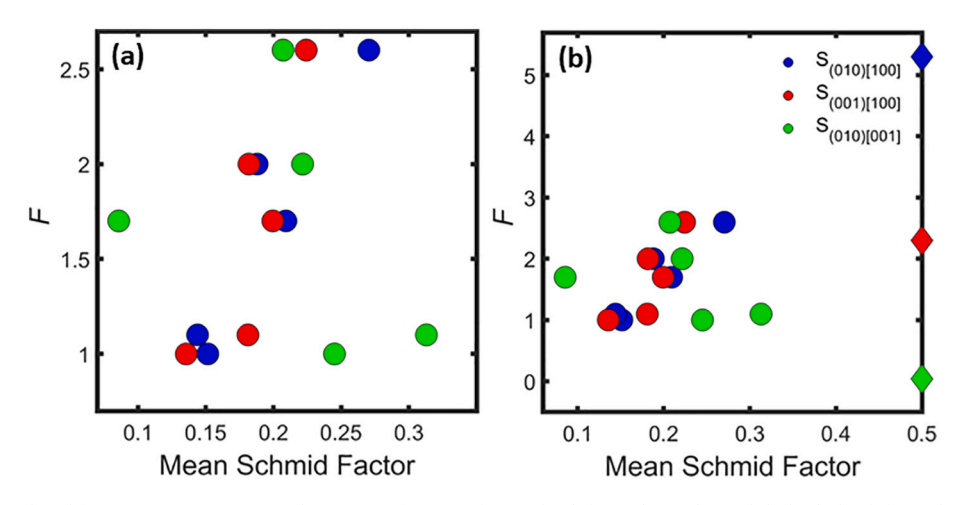


Fig. 5. Schmid factor maps for the dominant olivine slip systems, calculated from EBSD maps of deformed samples.



**Fig. 6.** Mean value of the Schmid factor versus strain rate enhancement factor, *F*, for (a) the deformed samples and (b) both the deformed samples (circles) and single crystals (diamonds – calculated from single-crystal flow laws of Bai et al. (1991)).

sample are necessary to quantify the microstructure and relate that microstructure to measured mechanical properties.

Overall, the mean values of the Schmid factor measured for each sample on the easiest slip systems, (010)[100] and the (100)[001] and [100](001) pair, correlate with the measured relative strength. We applied a modified power-law equation with the form,  $\dot{\varepsilon} = FA_0\sigma^n$  to analyze the relative strengths measured in our experiments, where  $A_0$  is a reference prefactor and F is the strain-rate enhancement factor. The value of  $A_0$  was taken as the prefactor calculated from the power-law fit with the stress exponent fixed to n=3.6 to the strongest orientation, where the [010] direction is dominantly aligned with the axis of the

sample. The strain-rate enhancement, *F*, is plotted in Fig. 6a against the mean value of the Schmid factor to evaluate the influence of CPO on anisotropic viscosity. A similar approach of comparing mean Schmid factor to strain-rate enhancement was used successfully by Azuma (1995) to interpret the mechanical behavior of ice with a preexisting CPO. A correlation between strain-rate enhancement and mean Schmid factors is clearly apparent in Fig. 6a. In Fig. 6b, the single-crystal flow laws from Bai et al. (1991) are added to highlight the relative strength of each of the slip systems, verifying that the trends in the data from this study are consistent with the relative strengths of the slip systems determined from single crystal deformation experiments. A simple

10<sup>-5</sup>

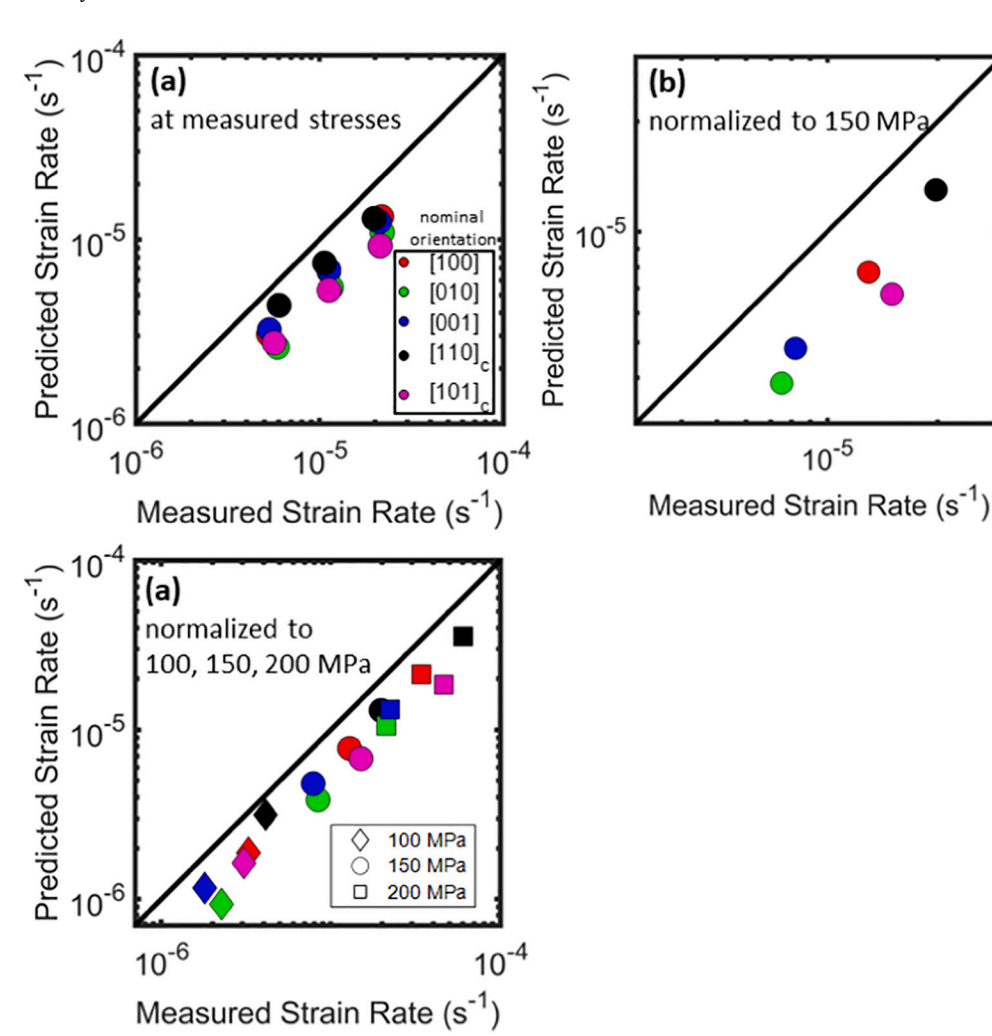


Fig. 7. Comparison of measured strain rate to predicted strain rate from a simplified effective-medium model incorporating the single-crystal flow laws of Bai et al. (1991), (a) calculated using the final stress of each strain rate step, (b) calculated normalizing data to 150 MPa using power-law fits to the data with n fixed at 3.6, and (c) calculated normalizing data to 100, 150, and 200 MPa using the experimentally measured stress exponent, n. The solid lines indicate exact correlation between the model and the data.

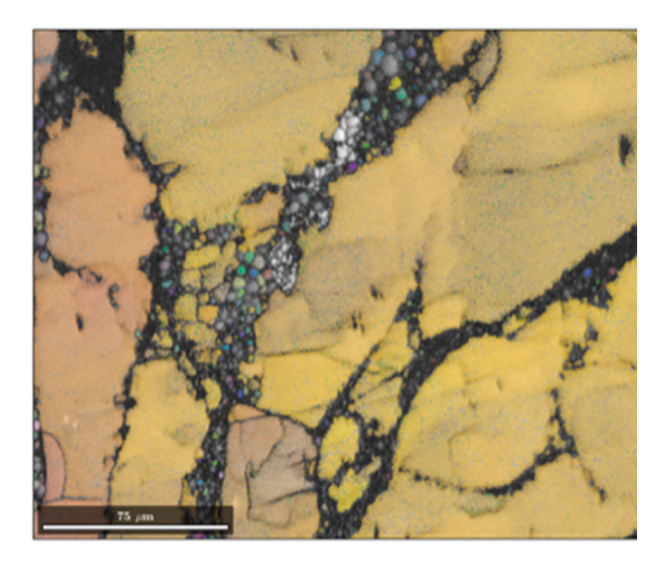


Fig. 8. High-resolution EBSD map (0.5 μm step size) of a portion of deformed sample material, shaded by band contrast and colored with IPF coloring of indexed olivine grains, demonstrating the presence of fine-grained material that fills relict fracture surfaces.

Table 2 Cricital resolved shear stresses for each slip system included in VPSC models.

Slip system	Critical resolved shear stress
(010)[100]	1
(001)[100]	1.5
(010)[001]	2
(100)[001]	3
(011)[100]	4
(110)[001]	6
$\{111\}\langle110\rangle$	β
$\{111\}\langle 011\rangle$	β
$\{111\}\langle 101\rangle$	β

mechanical model that incorporates single-crystal flow laws and measured values of Schmid factors is developed in the following section.

### 4. Discussion

Viscous anisotropy, with a maximum relative strength contrast of 2.6, was measured experimentally on a series of cores taken from a hand sample with an A/D-type CPO of intermediate fabric intensity. Broadly, the magnitude of the measured strengths of these samples were consistent with the results of similar experiments on nickel-jacketed samples by Keefner et al. (2011), intermediate relative to that measured from experiments on oriented single crystals and falling close to single crystals deformed in the [101]<sub>c</sub> orientation. Their study, however, did not

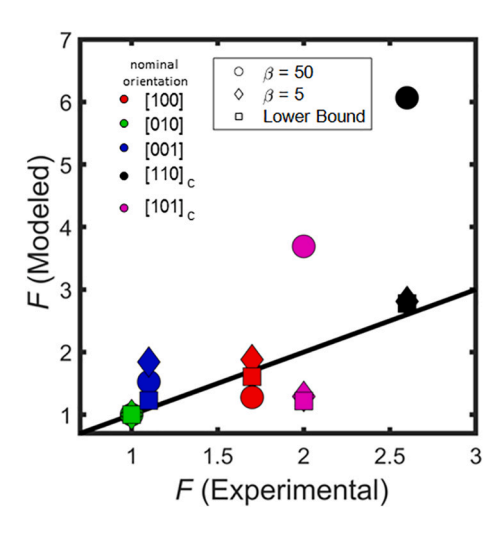


Fig. 9. Comparison of modeled and experimentally measured F for  $\beta=50$ ,  $\beta=5$ , and lower-bound models.

specifically address anisotropy due to preexisting CPOs. The magnitude of anisotropy that we measured experimentally is broadly consistent with multiscale numerical models that simulated deformation of dunites with fabrics of similar intensity and geometry, yielding calculated strength contrasts ranging from 1.5 to 3 (Knoll et al., 2009). Results from torsion experiments on samples of hot-pressed iron-rich olivine by Hansen et al. (2012b) predict a maximum strength contrast of roughly 5 for a similar fabric intensity. However, their experiments were performed in the dislocation-accommodated grain boundary sliding (disGBS) regime, and their samples also had strong grain shape preferred orientations (SPOs). Strong SPOs may lead to enhanced anisotropy in viscosity in the disGBS regime because alignment of grain boundaries may allow enhanced sliding in the direction of the long axes of grains. Therefore, one might expect some disagreement between our results and theirs.

Calibration of multiscale models, incorporating grain-scale to continuum-scale deformation, with experiments on dunites with a preexisting CPO is a promising future path for a detailed understanding of anisotropic viscosity. Hansen et al. (2016b), who applied this type of approach, found generally good agreement between experiment and grain-scale models. Comparisons of experimental data on hot-pressed iron-rich olivine to grain scale modeling was further explored Mameri et al. (2019), using VPSC simulations. VPSC simulations have been broadly applied to model the CPO evolution during deformation of olivine aggregates (Tommasi et al., 2000; Boneh et al., 2015). VPSC models use a simplified approach to account for strain compatibility and grain neighbor interactions. However, the limited data currently available that address this problem, combined with the complexity of multiscale modeling, motivates the use of a simpler framework for assessing the anisotropic viscosity of deformed dunites. Below we apply a simple mechanical model to evaluate viscous anisotropy in our experiments.

# 4.1. Effective medium theory for describing anisotropic viscosity

Stress–strain rate data from high-temperature deformation experiments on polycrystalline materials are often fit to a power-law relationship of the form

$$\dot{\varepsilon} = A' \sigma^n exp \left( -\frac{Q}{RT} \right), \tag{2}$$

where Q is the activation energy, T is the temperature, and R is the gas constant. This constitutive equation assumes that deformation occurs by a single, thermally activated mechanism and that the material is isotropic – simplifying the strain rate and stress tensors to single-valued

scalars in the principal reference frame of deformation. Since our experiments were all conducted at the same temperature, we use the further simplified expression given in eq. (1). However, non-linear, power-law behavior can be generalized for isotropic materials to an arbitrary spatial reference frame using the relation

$$\dot{\varepsilon}_{ij} = 3^{-(n+1)/2} \Phi \sigma_{\varrho}^{n-1} \sigma_{ij}, \tag{3}$$

where  $\sigma_e$  is the equivalent (von Mises) stress, which is proportional to the second invariant of the deviatoric stress tensor,  $\sigma_{ij}$  and  $\dot{\epsilon}_{ij}$  are the components of the deviatoric stress tensor and strain-rate tensors, respectively, and  $\Phi$  is a material dependent prefactor equal to the fluidity (the inverse of viscosity) when n = 1 (Karato, 2008, p. 37).

For linear creep mechanisms (n = 1), such as diffusion creep, this formalism can be simply extended to anisotropic materials, such that

$$\dot{\varepsilon}_{ij} = \Phi_{ijkl}\sigma_{kl},\tag{4}$$

where  $\Phi_{ijkl}$  is the fourth-rank fluidity tensor (Kohlstedt and Hansen, 2015). The components of the fluidity tensor are further restricted by material symmetry and volume conservation, such that for orthorhombic olivine, only six components are independent (Hansen et al., 2012b). However, extension to non-linear deformation is less straightforward. Kohlstedt and Hansen (2015) proposed the use of the constitutive equation

$$\dot{\varepsilon}_i = 3^{-(n+1)/2} \Phi_{ij} \sigma_e^{n-1} \sigma_j, \tag{5}$$

converting to Voigt notation, where stress and strain rate are represented as six-component vectors and the fluidity tensor is represented as a six-by-six second-rank tensor. This approach was applied by Király et al. (2020) to model the role of viscous anisotropy on deformation in Earth's mantle. This constitutive equation incorporates anisotropy into non-linear deformation but restricts the stress exponent to a single isotropic value. However, it is possible to imagine unrealistic outcomes using this functional form. For example, for a crystal with a single slip system, the above flow law implies that the strain rate resulting from dislocation motion on the single slip system will be influenced by shear stresses on orthogonal planes. Such complications highlight the difficulty of fully representing anisotropic non-linear deformation.

Regardless, for general scenarios, the fluidity tensor may be convenient because it can be reasonably implemented in large-scale geodynamic models (Mameri et al., 2021). The bulk fluidity tensor can be estimated using grain scale models, such as the VPSC method, or, simply constrained by commonly employed effective-medium theories (Mainprice and Humbert, 1994). In the bound of uniform stress (Sachs, 1928), the bulk fluidity tensor can be calculated from individual grain fluidity tensors by averaging over them, such that

$$\Phi_{ij} = \frac{1}{N} \sum_{c} \Phi_{ij}^{g},\tag{6}$$

where g is the grain index and N is the number of grains considered. Alternatively, in the bound of uniform strain rate (Taylor, 1938), the bulk fluidity tensor is calculated by averaging the inverse of the fluidity tensor of each grain, such that

$$\Phi_{ij} = \left(\frac{1}{N} \sum_{g} \left(\Phi_{ij}^{g}\right)^{-1}\right)^{-1}.\tag{7}$$

Empirical determination of the grain scale fluidity tensor from experimental data is a promising direction forward for analyzing anisotropic viscosity and assessing grain scale models, however, this analytical framework is considered still more complex than necessary for the analysis of our relatively simple set of experiments.

# 4.2. Simplified Schmid factor (resolved shear stress) model for describing anisotropic viscosity

We have applied a further simplified model to our experimental data, following the concepts of effective medium theory, described above, but limiting our analysis to the principal reference frame of deformation. We use Schmid's law to incorporate individual grain orientations and account for anisotropy. This model again reduces stress and strain rate to single-valued scalars and ignores cross terms that result from generalized anisotropy, wherein normal stresses can lead to shear strains. The analysis begins with the well-known Schmid's law, which states

$$\tau_r = S\sigma, \tag{8}$$

with

$$S = cos(\varphi)cos(\lambda), \tag{9}$$

where  $\tau_r$  is the resolved shear stress on the dislocation slip system being considered; S is the Schmid factor, which relates the orientation of the slip system to the orientation of the applied stress; and  $\phi$  and  $\lambda$  are the angles between the applied normal stress and the glide plane and the glide direction, respectively. The single-crystal flow laws from Bai et al. (1991), used in our analysis, were generated by axial compression experiments with known slip systems oriented for maximum resolved shear stress, such that S=0.5. These flow laws generally take the form of eq. (2). For an arbitrary compression orientation, considering only the contribution to axial shortening due to activity of the slip system isolated in the original compression experiments, the following modification to the flow law must be made:

$$\dot{\varepsilon}_{ss} = \sqrt{2}cos(\lambda)A'(2S\sigma)^n exp\left(-\frac{Q}{RT}\right)$$
 (10)

To further simplify our model such that strain rates are a simple function of Schmid factor, applied stress, and temperature, we make the approximation that the geometric term,  $\sqrt{2}cos(\lambda)$ , is equal to 1. This substitution implies that slip is evenly partitioned between shortening and lateral offset, which is only always true for the case of S=0.5. However, for a given Schmid factor, the even partitioning of strain between shortening and lateral offset is the average of possible outcomes and is, therefore, a reasonable approximation. This analysis also assumes that strains are small and that lattice rotation is unimportant. An equivalent substitution was used in the analysis of Raterron et al. (2011).

With this substitution, single-crystal flow laws developed from the results of axial compression experiments can be used to generate an approximate axial compression flow law for an arbitrary orientation. For the dominant slip systems in olivine, flow laws for the orientations  $[110]_c$ ,  $[101]_c$ , and  $[011]_c$  become functions of the appropriate Schmid factors and are summed to generate a flow law for a grain in an arbitrary orientation as follows:

$$\dot{\varepsilon}_1 = \dot{\varepsilon}_{[110]c} (S_{(010)[100]}, \sigma_{\text{applied}}, T, pO_2),$$

$$\dot{\epsilon}_2 = \dot{\epsilon}_{[101]c} \big( S_{(010)[100]} , \sigma_{applied}, T, pO_2 \big),$$

$$\dot{\varepsilon}_3 = \dot{\varepsilon}_{[011]c} (S_{(010)[100]}, \sigma_{applied}, T, pO_2),$$

and

$$\dot{\varepsilon}_{grain} = \dot{\varepsilon}_1 + \dot{\varepsilon}_2 + \dot{\varepsilon}_3. \tag{11}$$

We note that the paired (001)[100] and (100)[001] slip systems have the same Schmid factor and are both activated during [101]<sub>c</sub> compression, such that they cannot be accounted for separately. For a uniform grain size in the uniform-stress bound, the predicted aggregate strain rate is estimated as

$$\dot{\varepsilon}_{predicted} = \frac{1}{N} \sum \dot{\varepsilon}_{grain}. \tag{12}$$

In our analysis, we weight the contribution of each grain by its area in EBSD maps, thus approximating its fractional contribution to strain. This simple model ignores the necessity of strain compatibility and the role of neighbor–grain interactions.

When applied to our data, predicted strain rates from the model correlate well with the strain rates normalized to a constant stress, using power-law fits to the mechanical data. The correlation of the model to the relative strengths of differently oriented cores highlights the assertion that these experiments successfully measured viscous anisotropy in dunite with a preexisting CPO. However, at the stresses measured during our experiments, this analysis yields predicted strain rates that are consistently lower than those imposed in our experiments. This point is illustrated in Fig. 7a, where the correspondence between the data and the predictions from the model are plotted at the measured stress of each rate step (unnormalized). When normalized to a single stress (fixing the stress exponent to n = 3.6), the measured anisotropy is clear, and similar in magnitude to that predicted by the model, as demonstrated in Fig. 7b. Comparisons of the model predictions to the experimental data, normalized to 100, 150, and 200 MPa, using the experimentally determined stress exponent for each experiment (n) are also presented in Fig. 7c, further illustrating the correlation between the predicted and measured anisotropy. This result is further explored with VPSC calculations in the Appendix.

The observation that experimental strain rates are faster than predicted by the model, suggests that other mechanisms besides dislocation creep, accommodated by intragranular slip, are important to deformation. The simple model used in our analysis predicts an upper bound on deformation attributable to intracrystalline deformation; therefore, other deformation mechanisms, such as diffusion creep and disGBS, must be active to account for the observed deformation. A similar analysis of high-pressure deformation experiments on olivine aggregates presented by Raterron et al. (2019) made the same inference. It is likely that grain boundary sliding of finer grained material along relict fracture surfaces contributes to deformation, which may relax neighbor-grain restrictions. Also, samples may contain a small amount of melt, which would also reduce the viscosity.

# 4.3. Experimental limitations

The experimental results presented in this study demonstrate that the viscosity of dunites with a preexisting CPO is anisotropic; however, we note that the large grain size and complex microstructure of the starting material introduces some experimental limitations. After dehydration of alteration phases, a heavily fractured microstructure is left behind (Figs. 1a and 4). During hydrostatic annealing and deformation at 300 MPa confining pressure, these fractures close; however, fine-grained material is present along relict fracture interfaces. These fine-grained features are highlighted by the EBSD map presented in Fig. 8, made with a step size of 0.5 µm. While indexing of phases is poor in the finegrained regions, band contrast maps reveal the grain-scale microstructure. Most of these grains are less than  $5 \, \mu m$  and many were indexed as olivine. At the conditions of our experiments, diffusion creep and disGBS is likely active in these fine-grained regions. Some of the observed deformation is almost certainly accommodated by shear of fine-grained material along these relict fractures. However, bulk plastic flow was observed, and offsets along relict fractures at the edges of the sample were not observed after deformation, indicating that shear along relict fracture surfaces was limited. Further, the coincidence of relative strength and resolved shear stress on the dominant slip systems indicates that measured anisotropy was due to orientation of the preexisting CPO rather than secondary features. The large grain size of the dunite used in these experiments also makes sample-to-sample heterogeneity likely. Extension of this work might be best undertaken by identifying a finer

grained dunite with minimal alteration and fractures.

#### 5. Conclusions

We performed high-temperature deformation experiments on naturally sourced dunite with a preexisting CPO in order to investigate anisotropic viscosity. We measured a maximum effective viscosity contrast of 2.6 between the orientations tested when compared at constant stress. The dunite used in this study had an intermediate fabric intensity and, therefore, is likely to represent an intermediate viscous anisotropy. Further, the initial microstructure was heavily fractured, with fine-grained material along relict fracture interfaces, and may also contain a small amount of melt, both of which likely contribute to deformation and reduce the measured anisotropy. Therefore, our measurements likely represent a lower bound of the viscous anisotropy in Earth's mantle. A simplified effective-medium model fit the data reasonably well and demonstrated that viscous anisotropy was clearly measured in our experiments. This type of analysis may be a useful, simple formulation for analyzing anisotropic viscosity in future experimental studies. VPSC calculations, incorporating EBSD measurements made on our samples, also correlate well with our data, and support the interpretations drawn from our relatively simple analysis.

#### Credit author statement

The conception of this study was contributed by both authors. Experiments, data analysis, and drafting of the main body of the manuscript were performed by C.D.M. Assistance with sample preparation, critical review, and editing of the manuscript were performed by D.L.K.

# **Declaration of Competing Interest**

The authors declare that they have no known competing financial interests or personal relationships that could have appeared to influence the work reported in this paper.

# Acknowledgements

This work is supported in part by the Department of Energy National Nuclear Security Administration Stewardship Science Graduate Fellowship (to C.D.M) and the National Science Foundation [grant number EAR-1755805] (to D.L.K.). Parts of this work were carried out in the Characterization Facility, University of Minnesota, which receives partial support from NSF through the MRSEC program. We would like to thank Lars Hansen and Jessica Warren for supplying the hand sample used for deformation experiments. We would also like to thank Zachary Michels for his help with EBSD measurements and Lucan Mameri for his assistance with VPSC calculations. In addition, we would like to thank Andréa Tommasi and an anonymous reviewer for their helpful comments.

# Appendix A. VPSC calculations

A set of VPSC calculations were performed to further support the analysis of our experimental results. The tangent VPSC model is described by Lebensohn and Tomé (1993) and was applied to olivine by Tommasi et al. (2000) to predict CPO evolution in olivine aggregates. Later, the second order VPSC formulation was introduced (Ponte Castañeda, 2002), which was applied by Mameri et al. (2019) to model anisotropy in viscosity of experimentally deformed synthetic olivine aggregates. We modeled the results of our experiments using the second order VPSC method such that a direct comparison can be made to this earlier study. The grain orientations measured from EBSD maps of the experimentally deformed samples were used as the initial texture of the modeled aggregates. In the calculations, an axial compression stress boundary condition was imposed (consistent with experimental

conditions), and the modeled aggregate was deformed to 1% equivalent strain at a set rate. The nondimensional critical resolved shear stresses (CRSSs) used in our calculations are shown in Table 2 and are the same as used by Mameri et al. (2019). A stress exponent of n = 3 was used for all slip systems in the calculation. Pyramidal slip systems with a slip plane of {111} are included as "dummy" slip systems to close the yield surface and mimic additional isotropic strain accommodation mechanisms. Variation of the CRSS of these systems (β) changes the relative contribution of secondary isotropic mechanisms. We ran calculations using  $\beta = 50$  and  $\beta = 5$ , along with a lower-bound uniform stress model (Sachs, 1928) with the same CRSS values and boundary conditions as used for the VPSC models, to evaluate the role of secondary mechanisms in modeling our experimental results. Using the stresses predicted by our models we calculated the value of F for each model run, using a stress exponent for the aggregate of n = 3.5 and normalizing by the strength of the strongest sample. The results of these calculations are presented in Fig. 9.

Broadly, the results of these additional calculations correlate well with our experimental data and support the inference that strength variations that we measured experimentally are due to the anisotropy that results from the preexisting CPO. If isotropic mechanisms are limited ( $\beta=50$ ), the overall predicted magnitude of anisotropy is larger than measured experimentally. If secondary mechanisms are included ( $\beta=5$  and lower-bound models), the overall magnitude of anisotropy is better predicted for most sample orientations; however the sample oriented for compression along the  $[101]_{\rm c}$  direction is predicted to be relatively strong, in contrast to our experimental results. These results indicate that secondary mechanisms likely contribute to deformation in our experiments, relaxing neighbor–grain restrictions, which supports the applicability of the simplified Schmid factor model used to analyze our experimental results.

# References

Azuma, N., 1995. A flow law for anisotropic polycrystalline ice under uniaxial compressive deformation. Cold Reg. Sci. Technol. 23 (2), 137–147.

Bachmann, F., Hielscher, R., Schaeben, H., 2010. Texture analysis with MTEX – free and open source software toolbox. Solid State Phenom. 160, 63–68.

Bai, Q., Kohlstedt, D.L., 1992. High-temperature creep of olivine single crystals, 2. Dislocation structures. Tectonophysics 206 (1–2), 1–29.

Bai, Q., Mackwell, S.J., Kohlstedt, D.L., 1991. High-temperature creep of olivine single crystals 1. Mechanical results for buffered samples. J. Geophys. Res. 96 (B2), 2441–2463.

Becker, T.W., Kellogg, J.B., Ekström, G., O'Connell, R.J., 2003. Comparison of azimuthal seismic anisotrophy from surface waves and finite strain from global mantlecirculation models. Geophys. J. Int. 155 (2), 696–714.

Becker, T.W., Chevrot, S., Schulte-Pelkum, V., Blackman, D.K., 2006. Statistical properties of seismic anisotropy predicted by upper mantle geodynamic models. J. Geophys. Res. Solid Earth 111 (8), 1–16.

Boneh, Y., Morales, L.F., Kaminski, E., Skemer, P., 2015. Modeling olivine CPO evolution with complex deformation histories: implications for the interpretation of seismic anisotropy in the mantle. Geochem. Geophys. Geosyst. 16 (10), 3436–3455.

Bystricky, M., Kunze, K., Burlini, L., Burg, J.-P., 2000. High shear strain of olivine aggregates: rheological and seismic consequences. Science 290 (5496), 1564–1567.

Chatzaras, V., Kruckenberg, S.C., Cohen, S.M., Medaris, L.G., Withers, A.C., Bagley, B., 2016. Axial-type olivine crystallographic preferred orientations: the effect of strain geometry on mantle texture. J. Geophys. Re. Solid Earth 121 (7), 4895–4922.

Chopra, P.N., Paterson, M.S., 1984. The role of water in the deformation of dunite. Journal of Geophysical Research: Solid Earth 89 (B9), 7861–7876. In press.

Christensen, U.R., 1987. Some geodynamical effects of anisotropic viscosity. Geophys. J. R. Astron. Soc. 91 (3), 711–736.

Durham, W.B., Goetze, C., 1977. Plastic flow of oriented single crystals of olivine: 1. Mechanical data. J. Geophys. Res. 82 (36), 5737–5753.

Gatzemeier, A., Moorkamp, M., 2005. 3D modelling of electrical anisotropy from electromagnetic array data: hypothesis testing for different upper mantle conduction mechanisms. Phys. Earth Planet. Inter. 149 (3–4), 225–242.

Gatzemeier, A., Tommasi, A., 2006. Flow and electrical anisotropy in the upper mantle: finite-element models constraints on the effects of olivine crystal preferred orientation and microstructure. Phys. Earth Planet. Inter. 158 (2-4), 92–106.

Han, D., Wahr, J., 1997. An analysis of anisotropic mantle viscosity, and its possible effects on post-glacial rebound. Phys. Earth Planet. Inter. 102 (1–2), 33–50.

Hansen, L.N., Zimmerman, M.E., Kohlstedt, D.L., 2012a. The influence of microstructure on deformation of olivine in the grain-boundary sliding regime. J. Geophys. Res. Solid Earth 117 (9), 1–17.

Hansen, L.N., Zimmerman, M.E., Kohlstedt, D.L., 2012b. Laboratory measurements of the viscous anisotropy of olivine aggregates. Nature 492 (7429), 415–418.

- Hansen, L.N., Zhao, Y.H., Zimmerman, M.E., Kohlstedt, D.L., 2014. Protracted fabric evolution in olivine: implications for the relationship among strain, crystallographic fabric, and seismic anisotropy. Earth Planet. Sci. Lett. 387, 157–168.
- Hansen, L.N., Conrad, C.P., Boneh, Y., Skemer, P., Warren, J.M., Kohlstedt, D.L., 2016a. Viscous anisotropy of textured olivine aggregates: 2. Micromechanical model. J. Geophys. Res. Solid Earth 121 (10), 7137–7160.
- Hansen, L.N., Warren, J.M., Zimmerman, M.E., Kohlstedt, D.L., 2016b. Viscous anisotropy of textured olivine aggregates, part 1: measurement of the magnitude and evolution of anisotropy. Earth Planet. Sci. Lett. 445, 92–103.
- Hirth, G., Kohlstedt, D.L., 2003. Rheology of the upper mantle and mantle wedge: a view from the experimentalists. Geophys. Monogr. Inside Subduct. Fact. 138, 83–105.
- Hirth, G., Kohlstedt, D.L., 2015. The stress dependence of olivine creep rate: implications for extrapolation of lab data and interpretation of recrystallized grain size. Earth Planet. Sci. Lett. 418, 20–26.
- Ismaïl, W. Ben, Mainprice, D., 1998. An olivine fabric database: an overview of upper mantle fabrics and seismic anisotropy. Tectonophysics 296 (1–2), 145–157.
- Jung, H., Karato, S., 2001. Water-induced fabric transitions in olivine. Science 293 (5534), 1460–1463.
- Karato, S., 2008. Deformation of Earth Materials: An Introduction to the Rheology of Solid Earth, pp. 35–37.
- Katayama, I., Jung, H., Karato, S.I., 2004. New type of olivine fabric from deformation experiments at modest water content and low stress. Geology 32 (12), 1045–1048.
- Keefner, J.W., Mackwell, S.J., Kohlstedt, D.L., Heidelbach, F., 2011. Dependence of dislocation creep of dunite on oxygen fugacity: Implications for viscosity variations in Earth's mantle. J. Geophys. Res. 116.
- Király, Á., Conrad, C.P., Hansen, L.N., 2020. Evolving viscous anisotropy in the upper mantle and its geodynamic implications. Geochem. Geophys. Geosyst. 21 (10)
- Knoll, M., Tommasi, A., Logé, R.E., Signorelli, J.W., 2009. A multiscale approach to model the anisotropic deformation of lithospheric plates. Geochem. Geophys. Geosyst. 10 (8), 1–18.
- Kohlstedt, D.L., Hansen, L.N., 2015. Constitutive equations, rheological behavior, and viscosity of rocks. In: Treatise on Geophysics, , Second editionVol. 2. Elsevier B.V.
- Lebensohn, R.A., Tomé, C.N., 1993. A self-consistent anisotropic approach for the simulation of plastic deformation and texture development of polycrystals: application to zirconium alloys. Acta Metall, Mater. 41 (9), 2611–2624.
- Lev, E., Hager, B.H., 2008. Rayleigh-Taylor instabilities with anisotropic lithospheric viscosity. Geophys. J. Int. 173 (3), 806–814.
- Lev, E., Hager, B.H., 2011. Anisotropic viscosity changes subduction zone thermal structure. Geochem. Geophys. Geosyst. 12 (4), 1–9.
- Long, M.D., Becker, T.W., 2010. Mantle dynamics and seismic anisotropy. Earth Planet. Sci. Lett. 297 (3–4), 341–354.
- Long, M.D., Silver, P.G., 2009. Shear wave splitting and mantle anisotropy: measurements, interpretations, and new directions. Surv. Geophys. 30 (4–5), 407–461.
- Mainprice, D., Humbert, M., 1994. Methods of calculating petrophysical properties. Surv. Geophys. 15, 575–592.
- Mameri, L., Tommasi, A., Signorelli, J., Hansen, L.N., 2019. Predicting viscoplastic anisotropy in the upper mantle: a comparison between experiments and polycrystal plasticity models. Phys. Earth Planet. Inter. 286, 69–80.
- Mameri, L., Tommasi, A., Signorelli, J., Hassani, R., 2021. Olivine-induced viscous anisotropy in fossil strike-slip mantle shear zones and associated strain localization in the crust. Geophys. J. Int. 224 (1), 608–625.

- Mehl, L., Hacker, B.R., Hirth, G., Kelemen, P.B., 2003. Arc-parallel flow within the mantle wedge: evidence from the accreted Talkeetna arc, south central Alaska. J. Geophys. Res. 108 (B8).
- Mullet, B.G., Korenaga, J., Karato, S., 2015. Solid Earth Markov chain Monte Carlo inversion for the rheology of olivine single crystals. J. Geophys. Res. 120, 3142–3172.
- Paterson, M.S., 1990. Rock deformation experimentation. In: The Brittle-Ductile Transition in Rocks. Geophys. Monogr. Ser 56, pp. 187–194.
- Ponte Castañeda, P., 2002. Second-order homogenization estimates for nonlinear composites incorporating field fluctuations: I—theory. J. Mech. Phys. Solids 50 (4), 737–757.
- Pouilloux, L., Kaminski, E., Labrosse, S., 2007. Anisotropic rheology of a cubic medium and implications for geological materials. Geophys. J. Int. 170 (2), 876–885.
- Raterron, P., Chen, J., Geenen, T., Girard, J., 2011. Pressure effect on forsterite dislocation slip systems: Implications for upper-mantle LPO and low viscosity zone. Phys. Earth Planet. Inter. 188 (1–2), 26–36.
- Raterron, P., Bollinger, C., Merkel, S., 2019. Olivine intergranular plasticity at mantle pressures and temperatures. Compt. Rendus Geosci. 351 (2–3), 80–85.
- Ricoult, D.L., Kohlstedt, D.L., 1985. Experimental evidence for the effect of chemical environment upon the creep rate of olivine. In: Point Defects in Minerals. Geophys. Monogr. Ser 31, pp. 171–184.
- Sachs, G., 1928. The plastic deformation mode of polycrystals. Z. Ver. Dtsch. Ing. 72,
- Skemer, P., Katayama, I., Jiang, Z., Karato, S.-I., 2005. The misorientation index: development of a new method for calculating the strength of lattice-preferred orientation. Tectonophysics 411 (1-4), 157–167.
- Skemer, P., Warren, J.M., Hansen, L.N., Hirth, G., Kelemen, P.B., 2013. The influence of water and LPO on the initiation and evolution of mantle shear zones. Earth Planet. Sci. Lett. 375, 222–233.
- Tasaka, M., Zimmerman, M.E., Kohlstedt, D.L., 2015. Creep behavior of Fe-bearing olivine under hydrous conditions. J. Geophys. Res. Solid Earth 120, 6039–6057.
- Taylor, G., 1938. Plastic deformation of metals. 1. J. Inst. Met. 62, 307.
- Tielke, J.A., Hansen, L.N., Tasaka, M., Meyers, C., Zimmerman, M.E., Kohlstedt, D.L., 2016a. Observations of grain size sensitive power law creep of olivine aggregates over a large range of lattice-preferred orientation strength. J. Geophys. Res. Solid Earth 121 (2), 506–516.
- Tielke, J.A., Zimmerman, M.E., Kohlstedt, D.L., 2016b. Direct shear of olivine single crystals. Earth Planet. Sci. Lett. 455, 140–148.
- Tommasi, A., 1998. Forward modeling of the development of seismic anisotropy in the upper mantle. Earth Planet. Sci. Lett. 160 (1–2), 1–13.
- Tommasi, A., Mainprice, D., Canova, G., Chastel, Y., 2000. Viscoplastic self-consistent and equilibrium-based modeling of olivine lattice preferred orientations: Implications for the upper mantle seismic anisotropy. J. Geophys. Res. Solid Earth 105 (B4), 7893–7908.
- Tommasi, A., Knoll, M., Vauchez, A., Signorelli, J.W., Thoraval, C., Logé, R., 2009. Structural reactivation in plate tectonics controlled by olivine crystal anisotropy. Nat. Geosci. 2 (6), 423–427.
- Warren, J.M., Hirth, G., Kelemen, P.B., 2008. Evolution of olivine lattice preferred orientation during simple shear in the mantle. Earth Planet. Sci. Lett. 272 (3–4), 501–512.
- Wendt, A.S., Mainprice, D., Rutter, E., Wirth, R., 1998. A joint study of experimental deformation and experimentally induced microstructures of pretextured peridotites. J. Geophys. Res. 103, 18205–18221.